Characterization of surface-states in a hollow core photonic crystal fiber

ERICK LAMILLA,[1] MAICON S. FARIA,[1,2] IVAN ALDAYA,[1,3] PAULO F. JARSCHEL,[1] JULIÁN L. PITA,[4] AND PAULO DAINESE[1,*]

[1]*Institute of Physics "Gleb Wataghin," University of Campinas (UNICAMP), 13083-859, Campinas, SP, Brazil*
[2]*National Center for High Performance Computing in São Paulo (CENAPAD-SP),13083-889, Campinas, SP, Brazil*
[3]*Campus São João da Boa Vista, State University of São Paulo (UNESP), 13876-750, SP, Brazil*
[4]*School of Electrical and Computer Engineering, University of Campinas (UNICAMP), 13083-852, Campinas, SP, Brazil*
[*]*dainese@ifi.unicamp.br*

Abstract: Surface or edge states represent an important class of modes in various photonic crystal systems such as in dielectric topological insulators and in photonic crystal fibers. In the later, strong attenuation peaks in the transmission spectrum are attributed to coupling between surface and core-guided modes. Here, we explore a modified implementation of the spatial and spectral interference method to experimentally characterize surface modes in photonic crystal fibers. Using an external reference and a non-uniform Fourier transform windowing, the obtained spectrogram allows clear observation of anti-crossing behavior at wavelengths in which surface and core modes are strongly coupled. We also detect surface modes with different spatial symmetries, and give insight into mode families couple to the fundamental or high-order core modes, as well as the existence of uncoupled surface modes.

1.   Introduction

The surface of a photonic crystal can, under certain conditions, support localized surface modes, sometimes also referred to as edge or surface states [1, 2]. These surface modes can appear in different situations, such as at the interface between a photonic crystal and a homogeneous medium, at the interface between two different photonic crystals, or even at the surface of a defect inside a photonic crystal [1, 3, 4]. These particular modes have attracted significant attention more recently and novel proposals to exploit their attributes have been explored. One example is photonic topological edge states that have been demonstrated in a variety of photonic systems over the last years [5–8]. These topologically insulated modes may find interest in various applications given their robustness to structural defects in the photonic crystal [9–11]. In the area of integrated photonics, the possibility of using surface modes to efficiently couple light between conventional optical fibers and photonic crystal-based waveguides [12] or to enhance the quality factor in optical micro-cavities [13, 14] have been analyzed. Another area in which surface modes play a critical role is in photonic crystal fiber (PCF) [15]. Surface modes in PCFs have been used in plasmonic sensing for applications in medical diagnosis and detection of biomolecules and organic chemical compounds [16]. They have been also proved useful to understand the properties of atomic gases confined in hollow core (HC)-PCFs [17]. Lastly, the effects of surface modes in the transmission properties of HC fibers is fundamental in two ways [18, 19]. First, light coupled directly into a surface mode is generally strongly attenuated, given the fact that glass surface roughness causes significant scattering for modes with energy concentrated near the surface [20]. Another mechanism, perhaps even more important, is the existence of anti-crossing points in the dispersion curves due to mode coupling between a core-guided mode and different surface

modes [21]. This gives rise to symmetric and anti-symmetric core-surface modes that present a high overlap with the rough glass surface. As a result, at wavelengths in which strong coupling is observed, light launched into the core excites the coupled core-surface modes and is also strongly attenuated [21, 22]. Similar attenuation mechanisms in antiresonant HC fibers are also currently being discussed and analyzed [23, 24]. Precise engineering of the surface structure at the interface between the photonic crystal and the core modes can be very useful in controlling the coupling between the core and surface modes [25], and in some cases even possible to suppress it [26, 27]. The presence of coupled modes is generally assessed based on the existence of high attenuation peaks in the transmission spectrum, however a direct observation of the anti-crossing points and characterization of the coupled mode sructure is missing. Particularly, the identification of which surface modes couple with core-guided modes is difficult experimentally due to their highly-dispersive nature.

In this paper, we explore a modified implementation of the spatial and spectral (S^2) interference method [28] that employs an external reference and a non-uniform Fourier transform windowing. The method allows the direct observation of strong coupling between core-guided and surface modes. Our results reveal the existence of various surface modes with different spatial symmetries, and give insight into different mode families coupling to the fundamental and high-order core modes, as well as the existence of uncoupled surface modes. The developed modified method shows the mode structure and the anti-crossing behavior of the different coupled modes, and therefore can provide useful experimental information to controlling surface states not only in fibers but also in other guiding structures. The paper is organized as follows: in Section 2, we describe the modified S^2 implementation. In Section 3, the experimental recovery of different surface modes is presented and analyzed, and Section 4 concludes the paper.

2. Modified S^2 method for wavelength-resolved surface mode recovery

2.1. Experimental setup and fiber under test

S^2 imaging has been widely adopted for modal content characterization in few-mode and multi-mode fibers [29–32]. This method exploits the spectral interference between the excited modes to recover their amplitude and phase, as well as their relative power, without prior knowledge of the mode profile. The standard implementation of the S^2 method requires that most of the optical power is launched into the fundamental mode, which then serves as the reference to recover the other modes. The spatial interference pattern at the output of the fiber, therefore, is dominated by the beating between the reference fundamental mode and any other guided mode. Consequently, modes having little intensity overlap with the reference fundamental mode are difficult to be correctly recovered with this implementation. This is the case of surface modes in HC-PCFs. Another scenario where standard S^2 method results are not adequate is when the fundamental mode is not dominant. This is indeed the case at wavelengths in which strong coupling between the fundamental and surface modes occurs. As mentioned before, at these wavelengths the fundamental mode is strongly attenuated [21], and, hence, cannot be used as a reference. This can be overcome by using a fraction of the incoming laser power as an external reference in a Mach-Zehnder interferometer configuration, as shown in Fig. 1(a). Since the reference does not traverse the fiber, it is not affected by the high attenuation caused by surface-mode coupling, thus keeping its power constant over a broad wavelength range. In addition, the reference beam typically has a spot size much larger than the fiber fundamental mode at the output of the imaging system, and therefore provides a better signal-to-noise ratio for modes that do not overlap completely with the fundamental core mode. If needed, a beam expander can be implemented at the reference arm in order to further enlarge the spot size of the reference.

The system of Fig. 1(a) employed a tunable laser source (TLS) with a linewidth of 10 kHz and a wavelength sweep step of 8 pm. A polarization controller (PC) and a polarization beam splitter
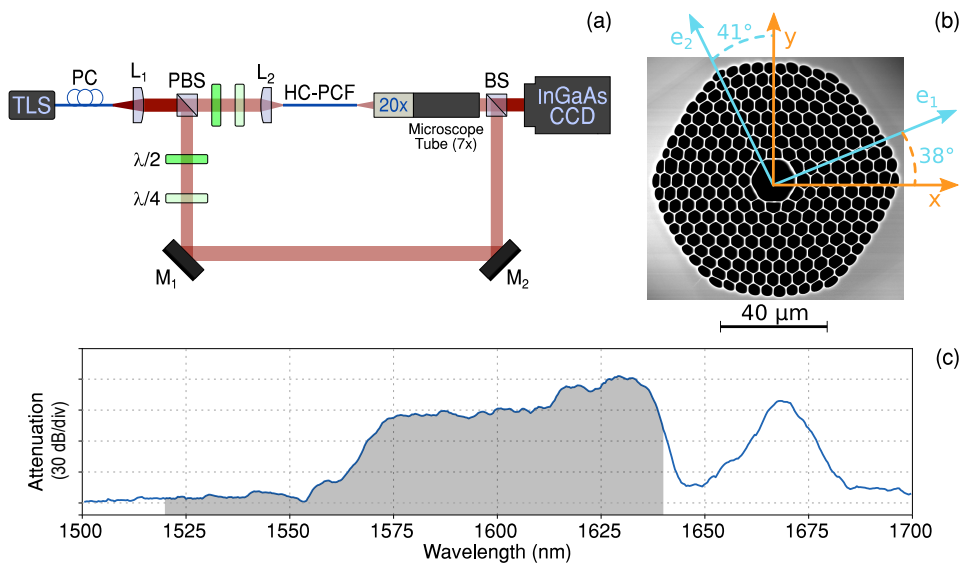
Fig. 1. (a) Setup of the S^2 method with external reference employed for mode coupling observation. TLS: tunable laser source; PC: polarization controller; $L_{1,2}$: lens; PBS: polarization beam splitter, $M_{1,2}$: mirror; HC-PCF: Hollow core photonic crystal fiber sample; and BS: beam splitter. (b) SEM image of the fiber with superimposed principal axis $\mathbf{e}_1$ and $\mathbf{e}_2$. (c) Attenuation spectrum of the HC-PCF. Modified S^2 method was performed in the highlighted region.

(PBS) at the input of the interferometer were used to control the relative power in the reference and test arms. The collimating lens L_1, with a focal distance of 16.5 mm, generated a reference beam with approximately 3.3 mm spot diameter. The state of polarization of the beams in the test and reference arms were controlled with two sets of $\lambda/2$ and a $\lambda/4$ wave-plates. We also carefully characterized the principal polarization axis in the fiber, $\mathbf{e}_1$ and $\mathbf{e}_2$, superimposed at Fig. 1(b) on the fiber cross-section image. The alignment at the input of the fiber was controlled by piezo-electric stages, allowing us to include lateral offset and, therefore, control the excitation of various modes. The fiber sample was ~98 cm long and it was kept straight and untwisted to avoid perturbation of the guided modes. The image of the fiber output beam was magnified using a magnification stage before being combined with the collimated reference beam via a beam splitter (BS). The combined beam was then projected on the image plane and detected with an InGaAs camera. In the results presented in the next section, the input polarization was set to match the principal axis $\mathbf{e}_1$ of the fiber at a 4 µm offset along this axis to strongly excite the surface modes. The fiber sample in this experiment was a 7-cell HC-PCF fabricated by Corning. The scanning-electron microscope (SEM) image shown in Fig. 1(b) was used to estimate the following fiber parameters: 16 µm air-core diameter, 4.9 µm cladding pitch and 92% air-fill fraction.

The imaging system at the output of the fiber arm induces a curved wavefront on the output beam, which when superimposed with the collimated reference beam leads to a circular interference pattern. In order to mitigate this effect, we adopted the approach proposed in [33], where the two beams are not combined perpendicularly but in a slightly oblique angle to a point that the spatial frequency is high enough to be easily filtered out either numerically or simply below the camera resolution. As in the standard S^2 method, the spatial beating pattern is captured using the InGaAs camera while the wavelength of the TLS is swept across a pre-defined window, and the data is post-processed to recover the mode profiles [28–30].

Fig. 1(c) shows the attenuation spectrum measured using a supercontinuum source and the well-known cut-back method on a 200 m long sample. It can be seen that the bandgap, corresponding to wavelengths with low-attenuation, spans from wavelengths shorter than 1500 nm up to wavelengths longer than 1700 nm with a broad high attenuation peak ranging from approximately 1550 nm to 1640 nm and a narrower peak between 1650 nm and 1680 nm. These peaks are associated with the presence of surface modes. The grey region identifies the wavelength range analyzed in the following sections, which is limited by the tunable laser. We will discuss a second important modification to the standard S^2 method in order to allow proper observation of surface modes and observe anti-crossing behavior when coupling to core modes occurs.

2.2. Wavelength-resolved mode analysis

In the standard S^2 method, as the laser frequency is swept, the beating period observed at any pixel in the camera is determined by the group delay difference between the fundamental and the secondary modes (typically higher-order core modes). When an external reference is added, a simple calculation shows that the time delay difference between the reference and the m-th mode of the fiber is given by:

$$\tau_{g,m}(\lambda) = \frac{1}{c} \left| n_{g,m}(\lambda)L - \Delta L \right|, \tag{1}$$

where L is the length of the fiber, c is the speed of light in the vacuum, λ is the wavelength, and ΔL represents the difference between the optical path in the reference and test arm (excluding the fiber length). This parameter accounts not only for the physical length difference but also for the optical path variation induced by the lenses and wave-plates. Since the measured wavelength window is relatively narrow, we can ignore the dispersion induced by the lenses. From now on, we refer to $\tau_{g,m}$ as differential group delay or simply differential delay of the m-th mode. The differential delay is generally expressed per unit of fiber length, which then acquires the form of: $\tau_{g,m}/L = 1/c \left| n_{g,m}(\lambda) - \Delta L/L \right|$. Note that the path difference leads to an offset in the differential delay proportional to $\Delta L/L$, which can be a useful tool to control the beating period in the experiment. For example, modes with very large group index require unpractical small wavelength steps to be well-resolved, and the offset $\Delta L/L$ can be adjusted to overcome this limitation.

To illustrate this discussion, we show numerically calculated dispersion curves for two types of surface modes in a HC-PCF. In Fig. 2(a) we show the dispersion relation for a surface mode (blue curve) that does not couple with the fundamental core mode (red curve), while in Fig. 2(b), we show the dispersion curves for a surface mode that indeed couples with the fundamental mode, leading to the characteristic anti-crossing behavior. Using the expression for $\tau_{g,m}/L$ with $L = 98$ cm (fiber sample length) and $\Delta L/L = 1.06$ (offset differential delay in our experiment), the differential group delay corresponding to the uncoupled and coupled modes are shown in Fig. 2(c) and Fig. 2(d), respectively. For the uncoupled modes, the two traces exhibit relatively low slope. As is typically the case, the differential delay for the surface mode is much higher than that of the core mode, leading in this case to a beating period of only 300 ps. With a wavelength sweep step of 8 pm, we still obtain about 3 points per cycle, above the Nyquist limit. If we were to have a lower offset, say slightly shorter reference arm $\Delta L/L = 0.94$, then the differential delay would be about 700 ps, and a much smaller step would be required. This illustrates the earlier comment that ΔL can be used to adjust the beating period. In the case of coupled modes, the differential group delays curves in Fig. 2(d) present a different behavior. A strong variation of $\tau_{g,m}/L$ with wavelength is observed near the anti-crossing point. Furthermore, it can be seen that the differential group delay rapidly drops to zero when $n_{g,m}(\lambda) = \Delta L/L$, and then is reflected off in the horizontal axis (which is simply a consequence of the modulus operation when calculating $\tau_{g,m}/L$). Fig. 2(e) shows the evolution of the normalized mode profiles (presented in the form of
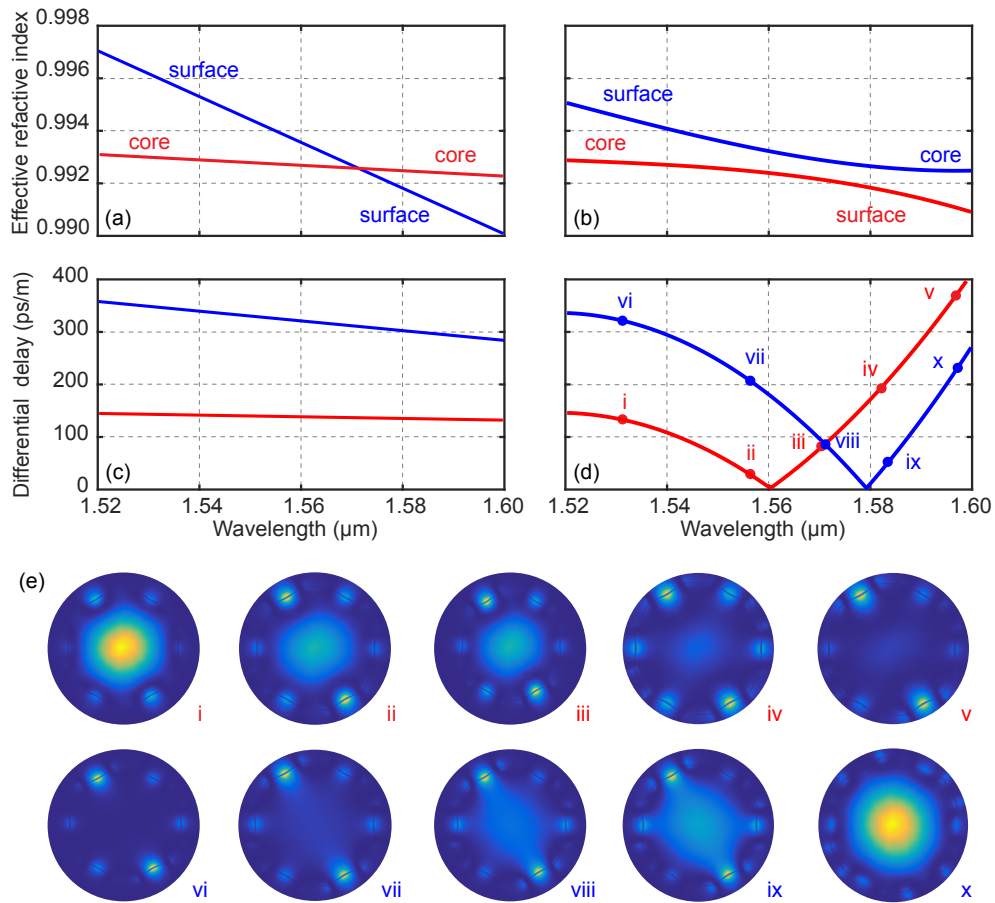
Fig. 2. (a),(b) Calculated dispersion for (a) a surface mode non-coupled with the fundamental mode and (b) a surface mode coupled with the fundamental mode. (c),(d) Differential group delay according to Eq. 1 corresponding to non-coupled and coupled surface mode shown in (a) and (b) respectively. (e) Evolution of the normalized mode profiles calculated at wavelengths indicated in (d).

square transverse field module) calculated at various wavelengths indicated in Fig. 2(d) before, near and after the anti-crossing point.

Typically, spectrograms with sliding window Fourier transform of the beating signal can be used to observe slight modifications of the group delay over the measured wavelength region [30–32, 34, 35]. Near anti-crossing points, however, the group index changes very rapidly with wavelength and so does the group delay as shown in Fig. 2(d). We show here that a non-uniform sliding window is required to appropriately recover the differential delay near anti-crossing points and therefore resolve surface-core coupled modes. This is the second modification to the method that is needed in order to resolve modes in coupled regions.

A fundamental limitation of any spectrogram-based analysis is the trade-off between the resolution in two domains, in our case, differential group delay and wavelength. A wide wavelength window leads to high resolution in differential group delay, but poor wavelength resolution and vice versa. This effect can be observed by comparing the experimental spectrograms shown in Fig. 3(a) and Fig. 3(b) for the previously described fiber. Both spectrograms were

computed from the same set of S^2 data using a wavelength sweep from 1520 nm to 1640 nm in steps of 8 pm, however, the wavelength window was set to 5 nm for Fig. 3(a) and 0.8 nm for Fig. 3(b). In the two cases, an overlap factor of 0.8 was employed (that is contiguous frequency windows are overlapped by 80%). Clearly, the wide wavelength window in Fig. 3(a) results in easily distinguishable traces with relatively flat differential delay, while high-slope curves appears blurred. On the other hand, in Fig. 3(b), a narrow wavelength window allows the identification of high-slope differential delay curves, corresponding to anti-crossing regions, but the poor time resolution avoids the correct discrimination between uncoupled modes (flat curves). In order to overcome this issue, we employed a wavelength window that varies from 5 nm for wavelength shorter than 1560 nm and 0.8 nm for wavelengths longer than 1570 nm. The resulting improved
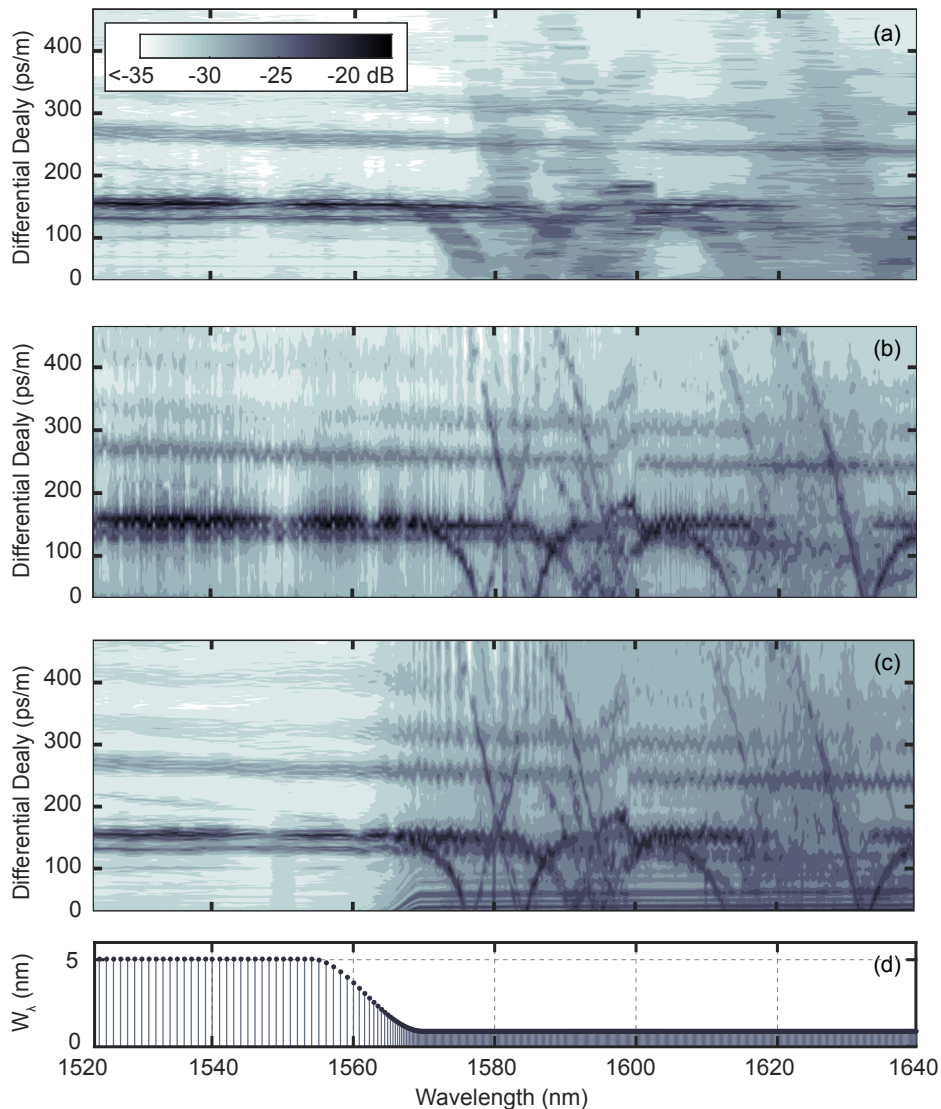

Fig. 3. (a),(b),(c) S^2 spectrograms for uniform wavelength window of (a) 5 nm and (b) 0.8 nm and for (c) variable wavelength window size. (d) Wavelength window size employed in (c) in terms of wavelength.

spectrogram is shown in Fig. 3(c), where both the coupled and uncoupled modes can be identified. For clarity purposes, in Fig. 3(d), the size of the wavelength window denoted by W_λ is presented. It can be seen that the transition was smoothed by using a raised cosine shape. In addition, since the overlap factor was relative to the size of the wavelength window, the density of windows for longer wavelength increases. Finally, as can be seen in Fig. 3(c), the experimental spectrogram reveals quite clearly the anti-crossing behavior corresponding to coupling between core and surface modes between 1570 and 1630 nm, which coincides with the high attenuation region of the fiber shown in Fig. 1(c). Another point that deserves noting is that experimental spectrograms show several low-slope lines at higher group delay differences. As it is shown in the next section, these lines correspond to surface modes that do not couple to core modes.

3. Results

We will analyze, first, the surface modes that are coupled to the core modes and, then, the modes that are not coupled.

3.1. Surface modes coupled to guided core modes

In order to analyze the mode coupling between surface and core modes, we used the aforementioned modified S^2 method to recover the mode profiles at different points of some selected traces, which are superimposed on the spectrogram in Fig. 4(a). First of all, the yellow and green lines correspond to the differential delay of the fundamental LP_{01}-like and the higher-order LP_{11}-like modes, respectively. As can be seen in Fig. 4(c) and 4(e), these modes can be recovered at different wavelengths and in discontinuous wavelength regions. The LP_{11}-like mode in Fig. 4(e) presents an apparent rotation, which can be explained by the presence of quasi-degenerate modes resulting from core imperfections and core asymmetry, causing the beating peaks to be very close. In the other two traces (light-blue and red), we study the coupling between the LP_{01}-like and the LP_{11}-like core modes and two surface mode profiles. The red line in Fig. 4(b) corresponds to the coupling observation between a surface mode and the fundamental LP_{01}-like core mode. The recovered mode profiles show remarkably the transition from uncoupled Fig. 4(b.i) and 4(b.ii) where the mode is clearly a core mode, reaching the anti-crossing point Fig. 4(b.iii) and 4(b.iv) where a coupled core-surface mode is observed, to finally after the anti-crossing point where the mode is completely a surface mode Fig. 4(b.v).

Similar behavior can be appreciated when the light-blue guiding line is followed. In this case, however, the mode coupling occurs between the high-order core LP_{11}-like mode and a surface mode, evolving from LP_{11}-like mode in Fig. 4(d.i) to a hybrid mode Fig. 4(d.iii) and 4(d.iv) and then follows to purely surface mode shown in Fig. 4(d.v). In both situations, it can be seen how the power is less concentrated in the hollow core and starts to be more concentrated in the interface between the core and the cladding. It is important to note that due to the nature of surface modes, a slight axial variation in the core-cladding interface will cause break of symmetry in the profile of the surface modes, as can be seen in Fig. 4(b.v) and 4(d.v)

(b) Tracking of coupling LP_{01}-like - surface mode

(c) Fundamental mode LP_{01}-like

(d) Tracking of coupling LP_{11}-like - surface mode

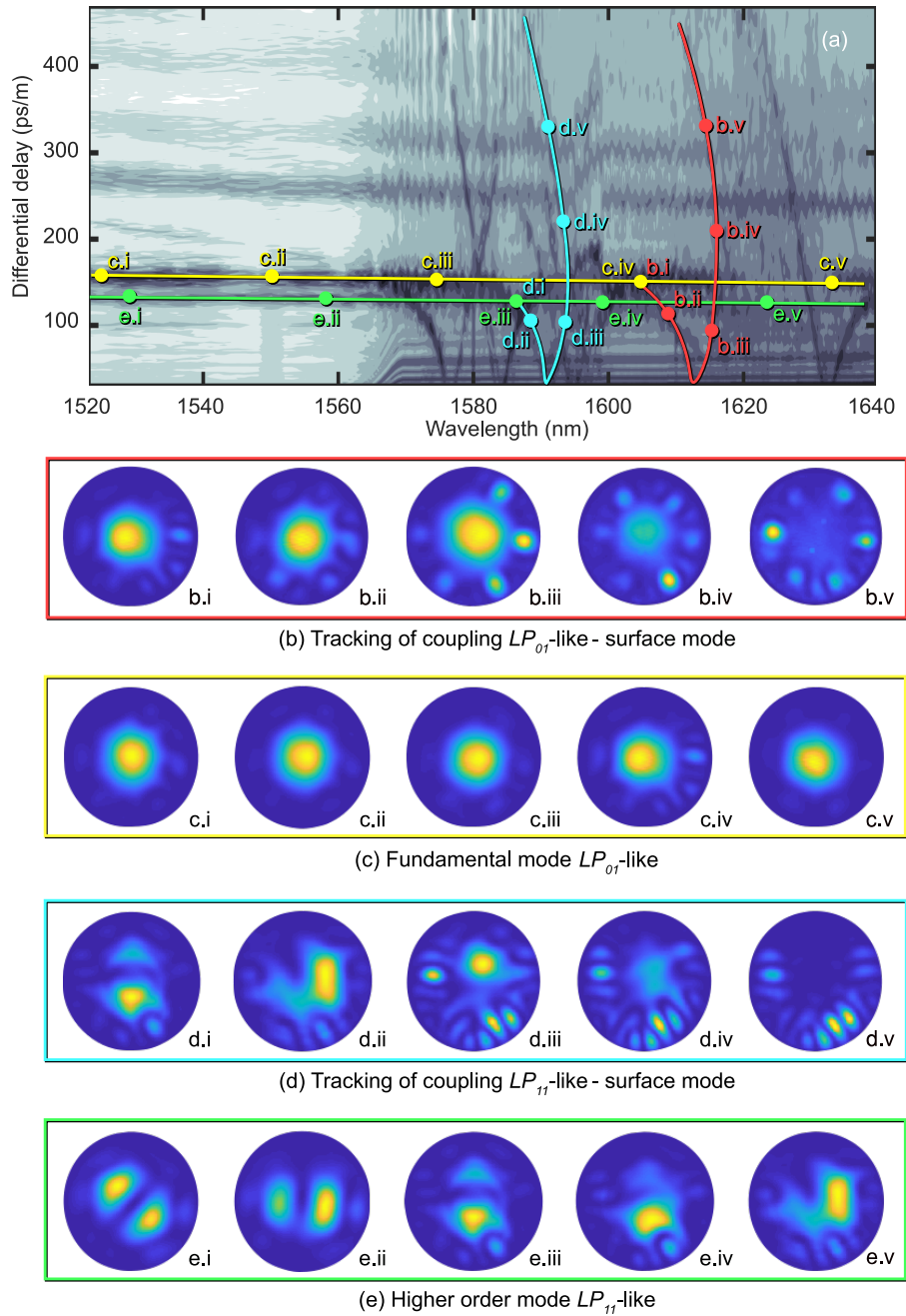(e) Higher order mode LP_{11}-like

Fig. 4. Surface modes coupled to core modes. (a) Spectrogram of Fig. 3(c) with superimposed traces. Normalized mode profiles at different points of the spectrogram corresponding to: (b) tracking of the coupling between surface mode and LP_{01}-like mode; (c) LP_{01}-like fundamental mode; (d) tracking of the coupling between surface mode and LP_{11}-like mode; and (e) LP_{11}-like higher order mode.

3.2. Surface modes not coupled to guided core modes

Not all surface modes, however, are coupled to the core modes. In particular, we identified three surface modes that do not present mode coupling. These surface modes, in contrast to those coupled to core modes, are less dispersive, leading to almost horizontal lines in the spectrogram and mode profiles that do not change in the observed wavelength range. Solid lines drawn on the spectrogram of Fig. 5(a) show the differential delay of these surface modes, whereas the corresponding mode profiles are presented in Fig. 5(b) - 5(d).
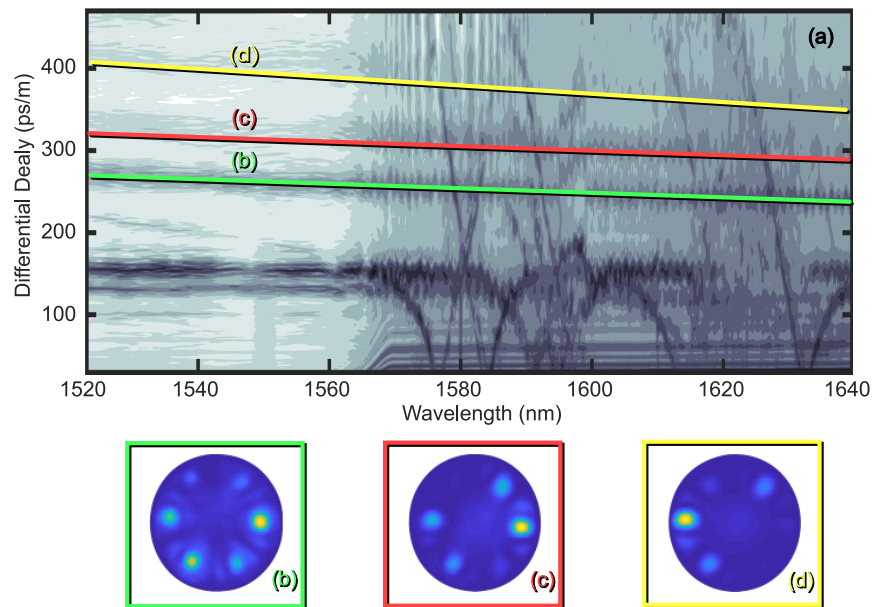

Fig. 5. Surface modes not coupled to core modes. (a) Spectrogram of Fig. 3(c) with superimposed traces. (b), (c), and (d) represent normalized mode profiles of the three identified surface modes that are not coupled to the core modes.

4. Conclusions

In this paper, we present an experimental characterization of surface modes in a 7-cell HC-PCF using a modified spatial and spectral interference method with an external reference and non-uniform Fourier transform window. The method allowed clear identification of several families of surface-modes, coupled and uncoupled, being able to recover well-defined mode profiles as well as to clearly observe anti-crossing behavior in the differential delay curves due to coupled of surface modes with core modes. Our observations confirm and provide insight into the specific mode structures of the coupled core-surface modes causing high-attenuation peaks in HC-PCF, and therefore can provide useful experimental information to controlling surface states.

References

1. P. Yeh, A. Yariv, and A. Y. Cho, "Optical surface waves in periodic layered media," Appl. Phys. Lett. **32**, 104–105 (1978).
2. J. D. Joannopoulos, S. G. Johnson, J. N. Winn, and R. D. Meade, *Photonic crystals: molding the flow of light* (Princeton university, 2011).
3. S. A. Skirlo, L. Lu, Y. Igarashi, Q. Yan, J. Joannopoulos, and M. Soljačić, "Experimental observation of large Chern numbers in photonic crystals," Phys. Rev. Lett. **115**, 253901 (2015).
4. C. M. Smith, N. Venkataraman, M. T. Gallagher, D. Müller, J. A. West, N. F. Borrelli, D. C. Allan, and K. W. Koch, "Low-loss hollow-core silica/air photonic bandgap fibre," Nature **424**, 657–659 (2003).
5. S. Longhi, "Bloch dynamics of light waves in helical optical waveguide arrays," Phys. Rev. B **76**, 195119 (2007).
6. R. Beravat, G. K. L. Wong, M. H. Frosz, X. M. Xi, and P. S. Russell, "Twist-induced guidance in coreless photonic crystal fiber: A helical channel for light," Sci. Adv. **2**, 1–5 (2016).
7. T. Weiss, G. K. L. Wong, F. Biancalana, S. M. Barnett, X. M. Xi, and P. S. Russell, "Topological Zeeman effect and circular birefringence in twisted photonic crystal fibers," J. Opt. Soc. Am. B **30**, 2921–2927 (2013).
8. X. M. Xi, G. K. L. Wong, M. H. Frosz, F. Babic, G. Ahmed, X. Jiang, T. G. Euser, and P. S. Russell, "Orbital-angular-momentum-preserving helical bloch modes in twisted photonic crystal fiber," Optica **1**, 165–169 (2014).
9. K. Fang, Z. Yu, and S. Fan, "Realizing effective magnetic field for photons by controlling the phase of dynamic modulation," Nat. Phot. **6**, 782–787 (2012).
10. M. C. Rechtsman, J. M. Zeuner, Y. Plotnik, Y. Lumer, D. Podolsky, F. Dreisow, S. Nolte, M. Segev, and A. Szameit, "Photonic Floquet topological insulators," Nature **496**, 196–200 (2013).
11. S. Mittal, S. Ganeshan, J. Fan, A. Vaezi, and M. Hafezi, "Measurement of topological invariants in a 2d photonic system," Nat. Phot. **10**, 180–183 (2016).
12. E. Moreno, F. J. García-Vidal, and L. Martín-Moreno, "Enhanced transmission and beaming of light via photonic crystal surface modes," Phys. Rev. B **69**, 121402 (2004).
13. S. Xiao and M. Qiu, "Optical microcavities based on surface modes in two-dimensional photonic crystals and silicon-on-insulator photonic crystals," J. Opt. Soc. Am. B **24**, 1225–1229 (2007).
14. D. Zhao and X. Jiang, "Vertical surface emitting open coupled-cavities based on photonic crystal surface modes," Appl. Opt. **47**, 1729–1733 (2008).
15. P. S. Russell, "Photonic-crystal fibers," J. Light. Technol. **24**, 4729–4749 (2006).
16. A. A. Rifat, F. haider, R. Ahmed, G. A. Mahdiraji, F. R. M. Adikan, and A. E. Miroshnichenko, "Highly sensitive selectively coated photonic crystal fiber-based plasmonic sensor," Opt. Lett. **43**, 891–894 (2018).
17. G. Epple, N. Y. Joly, T. G. Euser, P. S. Russell, and R. Löw, "Effect of stray fields on Rydberg states in hollow-core PCF probed by higher-order modes," Opt. Lett. **42**, 3271–3274 (2017).
18. R. Amezcua-Correa, F. Gérôme, S. G. Leon-Saval, N. G. R. Broderick, T. A. Birks, and J. C. Knight, "Control of surface modes in low loss hollow-core photonic bandgap fibers," Opt. Express **16**, 1142–1149 (2008).
19. R. Amezcua-Correa, N. G. R. Broderick, M. N. Petrovich, F. Poletti, and D. J. Richardson, "Optimizing the usable bandwidth and loss through core design in realistic hollow-core photonic bandgap fibers," Opt. Express **14**, 7974–7985 (2006).
20. B. Mangan, L. Farr, A. Langford, P. J. Roberts, D. P. Williams, F. Couny, M. Lawman, M. Mason, S. Coupland, R. Flea, H. Sabert, T. A. Birks, J. C. Knight, and R. S. J. Philip, "Low loss (1.7 db/km) hollow core photonic bandgap fiber," in *Optical Fiber Communication Conference,* (2004), p. PD24.
21. J. A. West, C. M. Smith, N. F. Borrelli, D. C. Allan, and K. W. Koch, "Surface modes in air-core photonic band-gap fibers," Opt. Express **12**, 1485–1496 (2004).
22. F. Couny, F. Benabid, P. J. Roberts, M. T. Burnett, and S. Maier, "Identification of Bloch-modes in hollow-core photonic crystal fiber cladding," Opt. Express **15**, 325–338 (2007).
23. A. Hartung, J. Kobelke, A. Schwuchow, K. Wondraczek, J. Bierlich, J. Popp, T. Frosch, and M. A. Schmidt, "Origins of modal loss of antiresonant hollow-core optical fibers in the ultraviolet," Opt. Express **23**, 2557–2565 (2015).
24. P. J. Roberts, D. P. Williams, B. J. Mangan, H. Sabert, F. Couny, W. J. Wadsworth, T. A. Birks, J. C. Knight, and P. S. Russell, "Realizing low loss air core photonic crystal fibers by exploiting an antiresonant core surround," Opt. Express **13**, 8277–8285 (2005).
25. R. Amezcua-Correa, N. G. R. Broderick, M. N. Petrovich, F. Poletti, and D. J. Richardson, "Design of 7 and 19 cells core air-guiding photonic crystal fibers for low-loss, wide bandwidth and dispersion controlled operation," Opt. Express **15**, 17577–17586 (2007).
26. H. K. Kim, J. Shin, S. Fan, M. J. F. Digonnet, and G. S. Kino, "Designing air-core photonic-bandgap fibers free of surface modes," IEEE J Quantum Electron. **40**, 551–556 (2004).
27. R. Amezcua-Correa, M. N. Petrovich, N. G. Broderick, D. J. Richardson, T. Delmonte, M. A. Watson, and E. J. O'Driscoll, "Broadband infrared transmission in a hollow-core photonic bandgap fibre free of surface modes," in *2006 European Conference on Optical Communications,* (2006), pp. 1–2.
28. J. W. Nicholson, A. D. Yablon, S. Ramachandran, and S. Ghalmi, "Spatially and spectrally resolved imaging of modal content in large-mode-area fibers," Opt. Express **16**, 7233–7243 (2008).
29. D. M. Nguyen, S. Blin, T. N. Nguyen, S. D. Le, L. Provino, M. Thual, and T. Chartier, "Modal decomposition technique for multimode fibers," Appl. Opt. **51**, 450–456 (2012).
30. J. Nicholson, L. Meng, J. Fini, R. Windeler, A. De Santolo, E. Monberg, F. DiMarcello, Y. Dulashko, M. Hassan,

and R. Ortiz, "Measuring higher-order modes in a low-loss, hollow-core, photonic-bandgap fiber," Opt. Express **20**, 20494–20505 (2012).

31. J. Jasapara and A. D. Yablon, "Spectrogram approach to s2 fiber mode analysis to distinguish between dispersion and distributed scattering," Opt. Lett. **37**, 3906–3908 (2012).

32. A. V. Newkirk, J. E. Antonio-Lopez, J. Anderson, R. Alvarez-Aguirre, Z. S. Eznaveh, G. Lopez-Galmiche, R. Amezcua-Correa, and A. Schülzgen, "Modal analysis of antiresonant hollow core fibers using S2 imaging," Opt. Lett. **41**, 3277–3280 (2016).

33. M. Lyu, Z. Lin, G. Li, and G. Situ, "Fast modal decomposition for optical fibers using digital holography," Sci Rep. **7**, 6556 (2017).

34. J. Carpenter, B. J. Eggleton, and J. Schröder, "Polarization-resolved cross-correlated (C2) imaging of a photonic bandgap fiber," Opt. Express **24**, 27785–27790 (2016).

35. J. Demas and S. Ramachandran, "Sub-second mode measurement of fibers using C2 imaging," Opt. Express **22**, 23043–23056 (2014).